Med Biol Eng Comput (2013) 51:207–218
DOI 10.1007/s11517-012-0985-6

ORIGINAL ARTICLE

Effect of head posture on the healthy human carotid bifurcation hemodynamics

Yannis Papaharilaou · Nicolas Aristokleous · Ioannis Seimenis · Mohammad Iman Khozeymeh · Georgios C. Georgiou · Brigitta C. Brott · Elena Eracleous · Andreas S. Anayiotos

Received: 26 April 2012 / Accepted: 29 October 2012 / Published online: 10 November 2012

Abstract Head and neck postures may cause morphology changes to the geometry of the carotid bifurcation (CB) that alter the low and oscillating wall shear stress (WSS) regions previously reported as important in the development of atherosclerosis. Here the right and left CB were imaged by MRI in two healthy subjects in the neutral head posture with the subject in the supine position and in two other head postures with the subject in the prone position: (1) rightward rotation up to 80°, and (2) leftward rotation up to 80°. Image-based computational models were constructed to investigate the effect of posture on arterial geometry and local hemodynamics. The area exposure to unfavorable hemodynamics, based on thresholds set for oscillatory shear index (OSI), WSS and relative residence time, was used to quantify the hemodynamic impact on the wall. Torsion of the head was found to: (1) cause notable changes in the bifurcation and internal carotid artery angles and, in most cases, on cross-sectional area ratios for common, internal and external carotid artery, (2) change the spatial distribution of wall regions exposed to unfavorable hemodynamics, and (3) cause a marked change in the hemodynamic burden on the wall when the OSI was considered. These findings suggest that head posture may be associated with the genesis and development of atherosclerotic disease as well as complications in stenotic and stented vessels.

Keywords Image-based CFD · Wall shear stress · Posture changes · Geometry characterisation · Atherosclerosis

Y. Papaharilaou
Institute of Applied and Computational Mathematics, Foundation for Research and Technology, Hellas, Nikolaou Plastira 100, Vassilika Vouton, 71 110 Heraklion, Crete, Greece

N. Aristokleous (✉) · M. I. Khozeymeh · A. S. Anayiotos
Department of Mechanical Engineering and Materials Science and Engineering, Cyprus University of Technology, 30 Archbishop Kyprianos Str., 3036 Lemesos, Cyprus
e-mail: n.aristokleous@cut.ac.cy

I. Seimenis
Laboratory of Medical Physics, Medical School, Democritus University of Thrace, Campus, 69100 Komotini, Greece

I. Seimenis · E. Eracleous
Ayios Therissos Medical Diagnostic Center, 92 Spyrou Kyprianou Ave, 2033 Nicosia, Cyprus

G. C. Georgiou
Department of Mathematics and Statistics, University of Cyprus, P.O. Box 20537, 1678 Nicosia, Cyprus

B. C. Brott · A. S. Anayiotos
Department of Medicine, The University of Alabama at Birmingham, 1530 3rd Avenue South Birmingham, Alabama 35294-1150, USA

1 Introduction

Each year ~795,000 people experience a new or recurrent stroke, and mortality data from 2007 indicate that stroke accounted for ~1 of every 18 deaths in the US [26]. The carotid bifurcation (CB) has been one of the most frequently studied sites evaluating the hemodynamic hypothesis of atherosclerosis. Earlier experimental studies in rigid and compliant models provided limited velocity and wall shear stress measurements and correlation of plaque location with regions of low and oscillating wall shear stress (WSS) [1, 8, 14, 17]. A complementary approach is the reconstruction of the complex three dimensional (3-D) flowfield of the CB using computational fluid dynamics (CFD) techniques. Perktold et al., provided

detailed numerical results of the 3D carotid bifurcation flowfield in idealized rigid [24] and compliant [25] wall models. These studies confirmed the existence of a complex flowfield at the bifurcation, with a high WSS region at the flow divider, and regions of low and oscillating WSS regions at the outer walls of the bifurcation.

The combination of 3D imaging techniques such as magnetic resonance imaging (MRI) and computer tomography (CT) with CFD allowed the construction of arterial models from anatomical images with more accurate geometric characteristics and boundary conditions [10, 28]. Such studies add the dimension of a patient-specific geometry to the carotid artery simulation. A recent study [6] including 61 subjects reported high reproducibility of CB models reconstructed from images obtained during routine contrast-enhanced MR angiography in the majority of cases. Hoi et al. [13] reported that the mild curvature that exists in the common carotid artery (CCA) of many subjects creates mild skewness of the CCA velocity profile. Zhang et al. [34] investigated the effect of geometry on the hemodynamics of the CB in 50 healthy subjects. Factor analysis was applied to a set of geometric variables to predict hemodynamic metrics related to shear and near wall residence times. The results showed that branch angle does not correlate with hemodynamic changes but other parameters, such as cross-sectional expansion and colinearity of the common and internal carotids have better correlation.

Several reports highlight the importance of motion and posture change on peripheral arteries such as the carotid, femoral, popliteal, and brachial, which may alter morphology and hemodynamic characteristics. The overviews by Taylor and Draney [29] and Steinman and Taylor [27] assessed the progress that has been achieved with image-based CFD studies in understanding the relationship between hemodynamics and development of disease. These authors specifically mention that it is important to better understand how local hemodynamics respond to normal physiological and postural variations. Cheng et al. [7] studied the in vivo deformations of the superficial femoral artery during maximum knee and hip flexion in seven healthy subjects, using magnetic resonance angiography. They reported significant morphological changes, such as shortening, lengthening and twisting clockwise and counter clockwise. These changes varied between subjects. Glor et al. [9] performed an ultrasound imaging study of the right CB and looked at the effects of leftwards head rotation in nine healthy subjects. They reported that head rotation changed the distribution of WSS and oscillatory index (OSI) primarily due to flow rate change in the rotated position. They also reported "planarification" of the CCA and changes in centerline location of the vessel with rotation.

Our recent work [3] in a group of ten healthy subjects imaged in the supine and prone position with head rotation to the right $\sim 80°$ demonstrated differences in the geometric parameters of the CB, with posture changes such as the bifurcation and internal carotid angles. In this study we seek to obtain a detailed description of the effects of leftwards and rightwards head rotation on both right and left CB morphology and local hemodynamics. Our hypothesis is that torsion of the head will affect the local hemodynamics by altering the magnitude and distribution of physiologically relevant hemodynamic variables such as WSS, OSI, wall shear stress temporal gradient (WSSTG) and relative residence time (RRT) that are generally associated with the genesis, development and proliferation of atherosclerosis.

2 Materials and methods

2.1 Subjects and imaging

Two healthy male volunteers in their mid-twenties were the subjects selected for this study. Both subjects were normotensives without known history of atherosclerotic disease. The right and left CB were MR imaged in the neutral head posture with the subject in the supine position and in two other head postures with the subject in the prone position: (1) rightward rotation (RR) up to 80°, and (2) leftward rotation (LR) up to 80° (Fig. 1). Supine and prone imaging sessions were carried out in a span of 2 weeks. The study was approved by the Cyprus Bioethics Committee and a consent form was obtained.

MRI images were obtained with a 3.0 Tesla scanner (Achieva, Philips Medical Systems, Best, The Netherlands) using the built-in quadrature RF body coil for proton excitation. A phased array eight-channel knee coil and a phased array two-channel superficial coil were used for signal detection in supine and prone position, respectively. A series of 100 thin sequential slices were obtained in the axial plane by 3D time-of-flight (TOF) methods, covering the CB of a healthy subject in the supine position. A 3D gradient-echo (GRE) pulse sequence (echo time (TE) = 3.5 ms, repetition time (TR) = 23 ms, a flip angle (FA) = 20°, $0.36 \times 0.36 \times 1.2$ mm^3 acquisition voxel and $0.2 \times 0.2 \times 0.6$ mm^3 reconstruction voxel) was employed. Multiple overlapping thin slab acquisition, a variable flip angle (16–24°) and gradient first moment nulling were applied to decrease the saturation effects of inflowing blood and reduce signal loss due to complex flow. The imaging sessions were carried out in a span of 2 weeks.

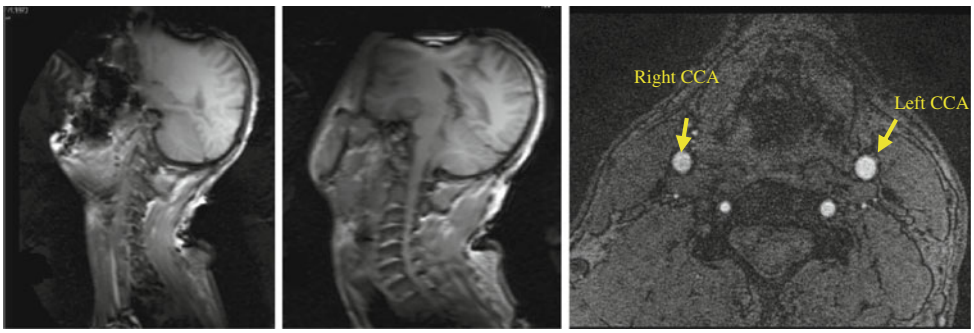

Fig. 1 *Left* to *Right* Neutral head position, prone rightwards rotated head position, and a TOF image used for segmentation

2.2 Surface reconstruction and geometric feature quantification

Segmentation and 3-D surface reconstruction of the acquired MR images were performed using ITK-Snap software [33]. The surface of the 3-D true vessel lumen was reconstructed from the manually segmented TOF images to extract the lumen contours. Pixel width constrained smoothing of the reconstructed surfaces was applied and smoothly matched cylindrical extensions of both inflow and outflow segments were added to facilitate the application of fully developed boundary conditions for the numerical simulation. In order to quantify the effects of head posture on the 3D geometry of the carotid bifurcation, the reconstructed 3D lumen surface was processed using VMTK [2] to extract the lumen centerlines and compute various geometric parameters.

Geometric features related to the CB such as the bifurcation angle, the ICA angle, the bifurcation area ratio, the ICA/CCA, ECA/CCA and ECA/ICA area ratios were computed based on the clipped CB geometries at the CCA3, ECA5 and ICA5 sections (more details can be found in [3]). The number in the specific locations CCA3, ECA5 and ICA5 indicates their geodesic distance along the centerline from reference points defining the boundaries of the CCA, and the ECA, ICA branches measured in units of maximally inscribed sphere radii as defined in [2]. The geometric parameter definitions are as follows: bifurcation angle is the angle between the projections of ICA and ECA vectors on to the bifurcation plane. ICA angle is the angle between the projections of CCA and ICA on to the bifurcation plane. Bifurcation area ratio was calculated as the sum of the ICA and ECA areas (levels ICA5 and ECA5) divided by the CCA area (level CCA3) ICA/CCA, ECA/CCA, and ECA/ICA diameter ratios were calculated as the square root of the corresponding area ratios, equivalent to vessel cross-sectional areas at levels CCA3, ICA5, and ECA5.

2.3 Mesh generation and flow computations

Previous studies have shown that, at regions of flow separation, low or oscillatory shear stress causes monocyte adhesion to the endothelium, an early stage in atherogenesis. Low shear stress leads to the expression of vascular cell adhesion molecule 1 (VCAM-1) a protein that mediates the adhesion of monocytes to the vascular endothelium [11], and a reduction in NO release [31]. WSSTG has also been related to the expression of atherogenesis-related genes in endothelial cells (ECs). Bao et al. [5] found that a temporal gradient in shear, stimulates the expression of monocyte chemoattractant protein-1 (MCP-1), a potent chemotactic agent for monocytes, and platelet-derived growth factor A (PDGF-A), a potent mitogen and chemotactic agent for smooth muscle cells. Higher values of WSSTG are, thus, likely to augment the development of atherosclerosis. WSSTG is the cycle-averaged magnitude of the time derivative of the instantaneous WSS and is expressed as:

$$\mathrm{WSSTG} = \frac{1}{T}\int_0^T \left|\frac{\partial \tau}{\partial t}\right| \mathrm{d}t \qquad (1)$$

where T is the flow-cycle period and $\boldsymbol{\tau}$ is the instantaneous WSS vector.

To investigate the complex 3-D flow dynamics, the Navier–Stokes equations were solved numerically using Fluent v12.1 (Ansys Inc.). The computational domain was spatially discretised with ICEM CFD v12.1 (Ansys Inc.) using $\sim 8.5 \times 10^5$ mixed type elements with higher grid density in the vicinity of the bifurcation and a viscous layer adjacent to the wall. The arterial wall was assumed rigid and blood was modeled as an incompressible Newtonian fluid with a density of 1.05 g cm^3 and a viscosity of 3.5 cP.

For practical reasons flow measurements were not obtained from the subjects in this study group. However, a physiological CCA flow waveform from a healthy male subject (Fig. 2), obtained previously by MR phase contrast velocimetry by our group, was used to prescribe the inlet boundary condition for all cases presented. By this method, we sought to exclude the effects of inter-individual CCA flow waveform variability, documented in the study of Glor et al. [9], from our results. For the same reason a constant 0.65/0.35 internal (ICA) to external carotid artery (ECA) flow split was applied. From the discrete Fourier series of

the volume flow rate, the fully developed time varying velocity profile was computed and was applied as the time-dependent inflow boundary condition. The spatiotemporally averaged Reynolds number of the prescribed waveform shown in Fig. 2 was $Re_{\mathrm{m}} = 305$ at the inlet and the Womersley parameter was $\alpha = 4.0$ (based on inlet radius $R = 2.96$ mm). A second-order upwind discretisation scheme was applied for the momentum equations and a second-order interpolation scheme for the pressure. The PISO algorithm was used for pressure velocity coupling. A time periodic solution was achieved after three flow cycles.

A time step of $\Delta t = 6.5 \times 10^{-6}$ normalized by the spatiotemporal mean inlet velocity per inlet diameter which resulted in 4,000 time steps per flow cycle and a spatial discretisation of the computational domain of $\sim 8.5 \times 10^5$ elements were applied. To test grid size independence we refined our initial mesh by reducing the mean cell center distance to double the number of elements in the computational domain from $\sim 8.5 \times 10^5$ to $\sim 1.7 \times 10^6$ and repeated our flow computations. Our results indicated a difference of less than 3.1 % in the computed wall shear stress magnitude integrated over the carotid bifurcation surface at peak systolic acceleration between the initial and refined meshes. A mesh of $\sim 8.5 \times 10^5$ elements was thus considered to provide sufficient computational accuracy and used as a guide in generating the meshes for all CB models used in this study. We also repeated our computations with half the initial time step resulting in 8,000 time steps per cycle and the difference found in the computed wall shear stress magnitude integrated over the carotid bifurcation surface at peak systolic acceleration was less than 2 %.

To obtain a measure of the oscillatory motion of the wall shear stress vector, a modified oscillatory shear index (OSI) was used based on the definition of Papaharilaou et al. [23], as both shear vector magnitude and direction change with time in a continuous fashion:

$$\mathrm{OSI} = \frac{\int_0^T w|\tau \cdot n_m|\mathrm{d}t}{\int_0^T |\tau \cdot n_m|\mathrm{d}t}, \qquad n_m = \frac{1}{T}\int_0^T \left(\frac{\tau}{\|\tau\|}\right)\mathrm{d}t \tag{2}$$

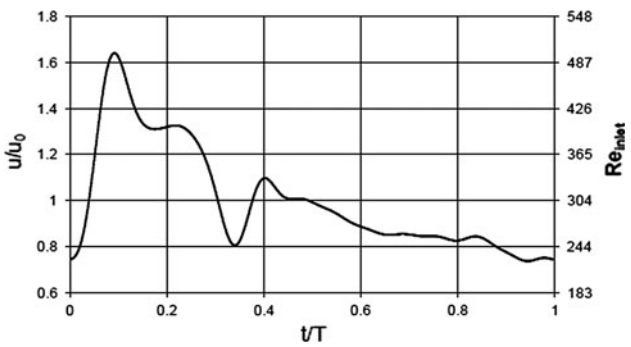

Fig. 2 MRI measured flow waveform imposed as inflow boundary condition for the computations

where T is the heart cycle period, $\boldsymbol{\tau}$ is the instantaneous wall shear stress vector, $\mathbf{n}_m$ is the mean shear direction and w is defined as $w = 0.5(1 - \cos a)$ where α is the angle between $\boldsymbol{\tau}$ and $\mathbf{n}_m$. The range of values for the modified index is $0 < \mathrm{OSI} < 0.5$ where 0 corresponds to unidirectional shear flow and 0.5 to the purely oscillatory shear case. To identify regions of low and oscillatory shear, we also consider a normalized OSI, (nOSI), which is calculated by dividing the OSI by the time-averaged WSS (TAWSS) magnitude normalized by the time-averaged inlet Poiseuille flow WSS. The WSSTG was also computed at each time step using a second-order central difference scheme.

We define unfavorable hemodynamics based on thresholds set for low TAWSS, high OSI, nOSI and RRT. The threshold for TAWSS was set to 0.4 Pa based on the study by Malek et al. [18]. Altering this value by ± 10 % and ± 20 % did not change the pattern in the results shown in Table 2. For high OSI we selected three threshold values (0.145, 0.238 and 0.3), the first two adopted from Lee et al. [16] and the last one added arbitrarily to assess the sensitivity of our results to the threshold. For nOSI the threshold (1.125) is calculated based on the respective thresholds for OSI and TAWSS and by normalizing the TAWSS threshold with the physiological level of TAWSS in arteries which is 1.5 Pa based on the study by Malek et al. [18]. The threshold values for RRT are computed using the following expression for RRT (Himburg et al. [12]):

$$\mathrm{RRT} = \frac{1}{(1 - 2\ (\mathrm{OSI}) \cdot \mathrm{WSS}_{\mathrm{poiseuille}})} \tag{3}$$

where $\mathrm{WSS}_{\mathrm{Poiseuille}}$ is the Poiseuille flow WSS at the inlet which here has a value of 0.267 Pa based on the applied cycle-averaged flow rate $Q = 4.72$ ml/s. From the three thresholds selected for OSI (0.3, 0.145, 0.238) and the expression for RRT we obtain the corresponding values for RRT 9.35, 5.29 and 7.14, respectively.

2.4 Reproducibility

In order to obtain an estimate of the uncertainty in the methodology used to quantify the hemodynamic burden for the cases studied and to assess the significance of our results, we repeated the whole process of imaging, segmentation, and flow simulation for subject II with the head in the neutral position. Repeat imaging was performed within 1 month from the original scan session using exactly the same setup and imaging protocol. Processing of the obtained images was carried out by the same individual in a similar manner to the original procedure. The absolute value of the difference between repeated measurements of subject II of the morphologic and hemodynamic metrics reported in this study are presented in Tables 1 and 2

Table 1 Geometric parameters for the three different head postures (*N* neutral head posture, *LR* leftward rotation, *RR* rightward rotation) and differences between LR and N (LR–N) and RR and N (RR–N), for the right (RCB) and left carotid bifurcation (LCB)

Geometric parameter		Subject I		Subject II	
		LCB	RCB	LCB	RCB
Angles (°)					
Bifurcation angle	LR–N	−6.3 ± 0.54	3.4 ± 0.54	−7.7 ± 0.54	9.5 ± 0.54
	N	54.65	40.74	45.34	31.09
	RR–N	−23.6 ± 0.54	16.8 ± 0.54	−5.7 ± 0.54	15.3 ± 0.54
ICA angle	LR–N	−2.1 ± 1.19	3.5 ± 1.19	−9.17 ± 1.19	17.9 ± 1.19
	N	26.3	22.73	28.88	15.73
	RR–N	−18.4 ± 1.19	12.7 ± 1.19	−16.2 ± 1.19	13.2 ± 1.19
Area ratios					
Bifurcation area ratio ($ICA_5 + ECA_5$)/CCA_3	LR–N	−0.03 ± 0.06	−0.15 ± 0.06	0.13 ± 0.06	0.35 ± 0.06
	N	1.21	1.34	1.14	1.0
	RR–N	0.27 ± 0.06	−0.11 ± 0.06	0.03 ± 0.06	0.21 ± 0.06
ICA_5/CCA_3	LR–N	−0.07 ± 0.02	0.08 ± 0.02	−0.08 ± 0.02	0.12 ± 0.02
	N	0.82	0.76	0.85	0.77
	RR–N	−0.1 ± 0.02	0.06 ± 0.02	−0.04 ± 0.02	0.12 ± 0.02
ECA_5/CCA_3	LR–N	0.04 ± 0.03	−0.17 ± 0.03	0.01 ± 0.03	0.12 ± 0.03
	N	0.74	0.87	0.64	0.63
	RR–N	−0.1 ± 0.03	−0.12 ± 0.03	0.03 ± 0.03	0.01 ± 0.03
ECA_5/ICA_5	LR–N	−0.1 ± 0.01	−0.1 ± 0.01	0.1 ± 0.01	0.03 ± 0.01
	N	0.9	1.14	0.75	0.82
	RR–N	0.0 ± 0.01	−0.22 ± 0.01	0.07 ± 0.01	−0.1 ± 0.01

Whole process reproducibility for each parameter is also reported to the right of symbol (±) for reference

herein (values to the right of symbol ±) as an estimate of whole process reproducibility.

3 Results

Our analysis of the reconstructed models of the left and right carotid arteries for the rightwards and leftwards head rotation revealed marked morphological differences compared to the neutral head posture for the two subjects presented in Table 1. Geometric features related to the CB such as the bifurcation angle, the ICA angle, the bifurcation area ratio, the ICA/CCA, ECA/CCA and ECA/ICA area ratios were computed based on the clipped CB geometries at the CCA3, ECA5 and ICA5 sections. The changes in the bifurcation and ICA angles due to head rotation reported in Table 1 are well above the reproducibility of our method. Of note is the reduction in both the bifurcation and ICA angles caused by head torsion both rightwards and leftwards that occurs for the left CB in both subjects. This change ranges from 6° to 24° for the bifurcation angle and from 2° to 18° for the ICA angle. The effect is opposite for the right CB where an increase between 3° and 17° of the bifurcation angle and 3° and 18° of the ICA angle with head torsion is observed. These changes are significant considering that a mean values for the bifurcation and ICA angles in the neutral position is ∼42° and ∼23°, respectively. Another observation is that there is a larger effect on the bifurcation and ICA angles due to rightwards as compared to the leftwards rotation of the head. The difference in cross-sectional area ratios for CCA, ICA and ECA found as a result of head torsion was considered relatively small to moderate but still in most cases well above our whole process reproducibility.

A quantification of the impact on the atherosclerotic burden associated with head posture changes is presented in Table 2. For each case the relative area exposed to unfavorable hemodynamics was obtained by dividing the exposed area to the CB wall surface area clipped at the CCA3, ECA5 and ICA5 sections as reported in Lee et al. [16]. Differences in the exposure area due to head rotation are reported in reference to the reproducibility of the 'whole process' methodology. It is worth noting that, in almost all cases considered, there are differences in the magnitude of the respective metric between the neutral and leftwards and rightwards head postures. Considering the whole process reproducibility, the reported changes represent a marked alteration in hemodynamic burden when the wall exposure to OSI and nOSI are considered. The changes in the computed flow field due to head torsion

Table 2 Area exposed to unfavorable hemodynamics normalised by the total surface area bounded by CCA3, ECA5, ICA5 for the three head postures considered (*N* neutral head posture, *LR* leftward rotation, *RR* rightward rotation) and differences between LR and N (LR–N) and RR and N (RR–N) for the right (RCB) and left carotid bifurcation (LCB)

		Subject I		Subject II	
		LCB	RCB	LCB	RCB
TAWSS < 0.32 (Pa)	LR–N	−0.02 ± 0.025	−0.1 ± 0.025	−0.02 ± 0.025	0.01 ± 0.025
	N	0.23	0.29	0.25	0.23
	RR–N	−0.05 ± 0.025	0 ± 0.025	−0.08 ± 0.025	0.07 ± 0.025
TAWSS < 0.4 (Pa)	LR–N	−0.01 ± 0.034	−0.1 ± 0.034	0 ± 0.034	0.03 ± 0.034
	N	0.28	0.36	0.29	0.27
	RR–N	−0.06 ± 0.034	−0.01 ± 0.034	−0.1 ± 0.034	0.08 ± 0.034
TAWSS < 0.48 (Pa)	LR–N	−0.01 ± 0.038	−0.1 ± 0.038	0 ± 0.038	0.05 ± 0.038
	N	0.33	0.43	0.35	0.32
	RR–N	−0.07 ± 0.038	−0.01 ± 0.038	−0.13 ± 0.038	0.08 ± 0.038
OSI > 0.3	LR–N	−0.01 ± 0.001	−0.01 ± 0.001	−0.03 ± 0.001	0.01 ± 0.001
	N	0.03	0.02	0.04	0.02
	RR–N	−0.02 ± 0.001	0 ± 0.001	−0.01 ± 0.001	0.03 ± 0.001
OSI > 0.145	LR–N	0 ± 0.02	−0.03 ± 0.02	−0.05 ± 0.02	−0.02 ± 0.02
	N	0.09	0.09	0.14	0.11
	RR–N	−0.02 ± 0.02	−0.01 ± 0.02	−0.01 ± 0.02	0.05 ± 0.02
OSI > 0.238	LR–N	−0.02 ± 0.004	−0.02 ± 0.004	−0.04 ± 0.004	0.01 ± 0.004
	N	0.05	0.04	0.07	0.04
	RR–N	−0.03 ± 0.004	−0.01 ± 0.004	−0.01 ± 0.004	0.05 ± 0.004
nOSI > 1.125	LR–N	−0.01 ± 0.01	−0.02 ± 0.01	−0.06 ± 0.01	−0.01 ± 0.01
	N	0.07	0.06	0.11	0.08
	RR–N	−0.02 ± 0.01	0.01 ± 0.01	−0.02 ± 0.01	0.05 ± 0.01
RRT > 9.35	LR–N	−0.02 ± 0.055	−0.03 ± 0.055	−0.06 ± 0.055	−0.02 ± 0.055
	N	0.11	0.10	0.15	0.12
	RR–N	−0.03 ± 0.055	0.01 ± 0.055	−0.03 ± 0.055	0.05 ± 0.055
RRT > 5.29	LR–N	−0.01 ± 0.047	−0.09 ± 0.047	−0.05 ± 0.047	−0.02 ± 0.047
	N	0.16	0.21	0.21	0.17
	RR–N	−0.03 ± 0.047	−0.02 ± 0.047	−0.06 ± 0.047	0.07 ± 0.047
RRT > 7.14	LR–N	0.02 ± 0.05	−0.06 ± 0.05	−0.06 ± 0.05	−0.02 ± 0.05
	N	0.10	0.15	0.18	0.14
	RR–N	0 ± 0.05	0 ± 0.05	−0.05 ± 0.05	0.07 ± 0.05

Whole process reproducibility for each hemodynamic index is also reported to the right of symbol (±) for reference

observed in the reconstructed models of subjects I and II are depicted in Figs. 3, 4, 5 and 6, respectively. Contour plots of the TAWSS, nOSI, OSI, RRT and WSSTG are shown for the different head positions of the two cases studied.

For subject I and for OSI and nOSI parameters a different pattern is noted where a reduction of arterial wall exposure to unfavorable hemodynamics occurs as a result of leftward rotation of the right CB and of rightward rotation of the left CB which range from 33 to 50 % and from 22 to 60 %, respectively, compared to the neutral position. In the later case we also note a marked change in the distribution of the wall exposure to unfavorable hemodynamics as shown in Figs. 3 and 4 where contour lines for OSI = 0.238 and nOSI = 1.125 are depicted to mark the boundaries of the wall regions exposed to highly oscillatory or low and oscillatory shear stress, respectively. RRT-related graphs in Figs. 3 and 4 present similar distribution patterns as those for OSI and nOSI. This is not unexpected as these parameters are measures of similar hemodynamic features. It also worth noting that in most cases considered the temporal gradients of WSS in the vicinity of the CB are not strongly affected by head torsion. This could be explained by the fact that WSSTG is primarily sensitive to the frequency content of the flow waveform which in this study was kept the same for all cases considered. Finally, it is also of interest to note that differences in the spatial distribution of RRT as depicted in

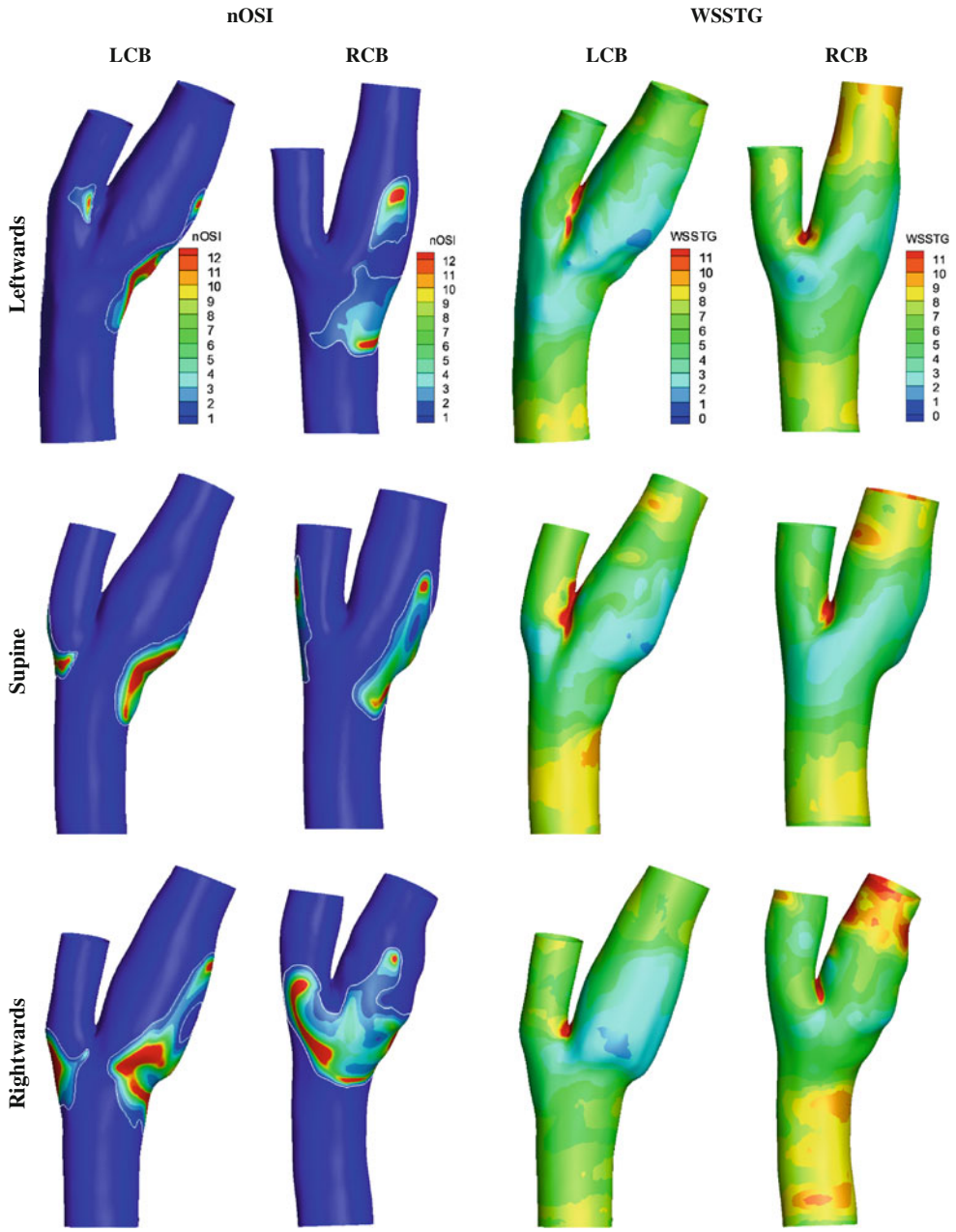

Fig. 3 *Contour plots* of time-averaged nOSI and WSSTG for the right and left carotid in the neutral, leftward and rightward rotated head position for subject I. nOSI = 1.125 *contour lines* are shown

Figs. 4 and 6 are not associated with notable changes in the total hemodynamic burden on the wall as shown in Table 2.

Based on the results obtained from subject II presented in Table 2 for the OSI and nOSI parameters a marked reduction is found in the hemodynamic burden caused by leftward rotation of the left CB which ranged from 35 to 75 % compared to the neutral position. We also note a marked increase in hemodynamic burden caused by rightwards rotation of the right CB which ranged from 45 to 125 % compared to the neutral position. These findings are illustrated in Figs. 5 and 6. Of note is the marked change in the nOSI distribution caused by the rightwards rotation of the right CB where there is both a relatively large increase in the surface area exposed to low and highly oscillatory shear stress and a large change in the distribution of the affected wall regions in the rotated head posture.

4 Discussion

The results of this study indicate that torsion of the neck associated with head rotation to the right or to the left may

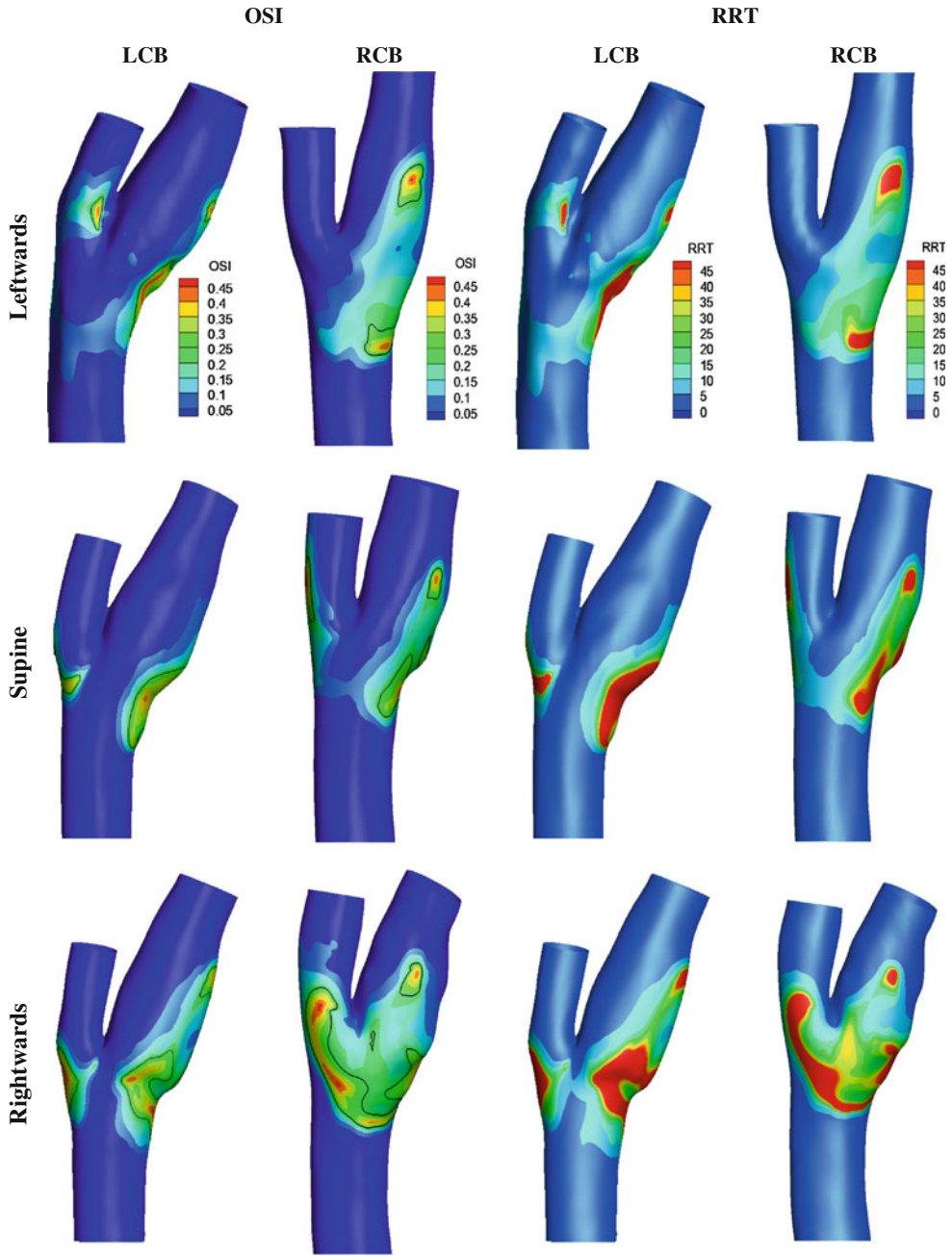

Fig. 4 *Contour plots* of time-averaged OSI and RRT for the right and left carotid in the neutral, leftward and rightward rotated head position for subject I. OSI = 0.238 *contour lines* are shown

cause marked changes in CB morphology and hemodynamics. Our findings suggest that head rotation reduces the hemodynamic burden for subject I both for left and right CB, and for the left CB of subject II. For the right CB of subject II, we found that leftwards rotation reduces and rightwards rotation increases the hemodynamic burden. We have shown previously [3] that the variation caused by head rotation on CB geometry is subject specific. Here our results suggest that not only the effect of head torsion on the CB hemodynamics is subject specific which is in agreement with the findings of Glor et al. [9] but also varies between right and left CB for the same subject. Glor et al. [9] only looked into the effects of head rotation on geometry and hemodynamics for the right CB and for leftwards rotation of the head. Moreover, their study included nine healthy subjects selected to have a bifurcation point relatively low in the neck due to accessibility constraints associated with their imaging method (3D Ultrasound). They regarded the changes in cross-sectional areas of the CB vessels due to head rotation as insignificant

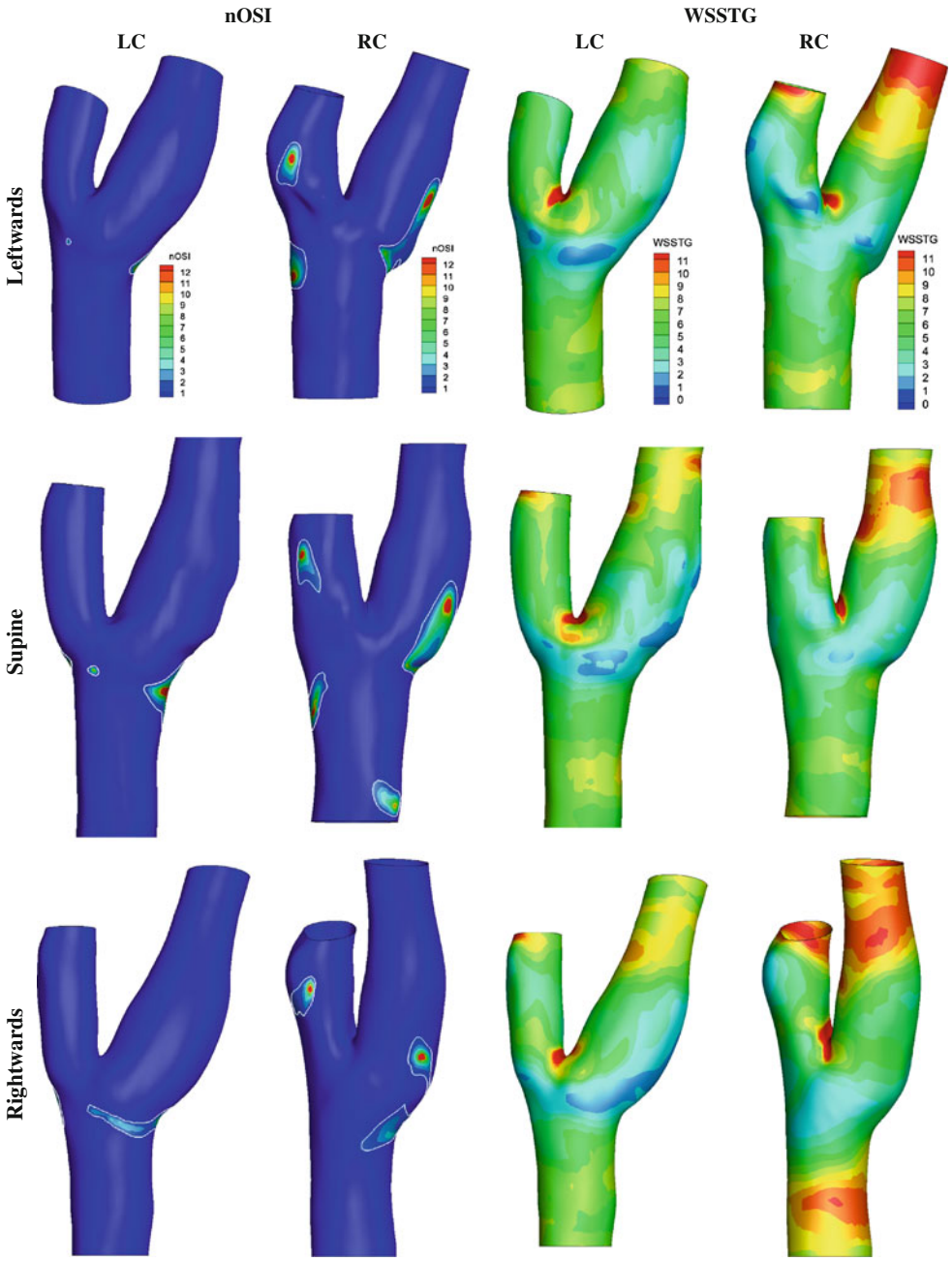

Fig. 5 *Contour plots* of time-averaged nOSI and WSSTG for the right and left carotid in the neutral, leftward and rightward rotated head position for subject II. nOSI = 1.125 *contour lines* are shown

considering the uncertainty of their methods. However, this may also be due to the lack of sufficient sensitivity of their measurement technique as they admit. Our results also indicate that cross-sectional changes with head rotation are small to moderate in most cases but above the reproducibility of our methodology.

Glor et al. [9] reported significant changes in the relative positions of the CCA, ICA and ECA quantified on the basis of the centerlines extracted from the respective vessels. Such CB shape alterations, quantified by the bifurcation and ICA angles, were also reported in our previous work with a greater number of subjects [3]. This study confirms that this occurs in both the right and left CB and independent of the head rotation direction. Glor et al. [9] reported significant changes in the distribution patterns of TAWSS and OSI with head rotation. Since, however, subject-specific flow waveforms were applied as boundary conditions in their numerical simulations, both geometric and flow rate changes contributed to the differences found. To isolate the effect of head rotation on the hemodynamics from the variations in flow rate, we imposed the same inlet boundary condition and prescribed a constant ECA/ICA flow split for all cases. This, however, excludes the mild influence of head posture on the inlet conditions which was

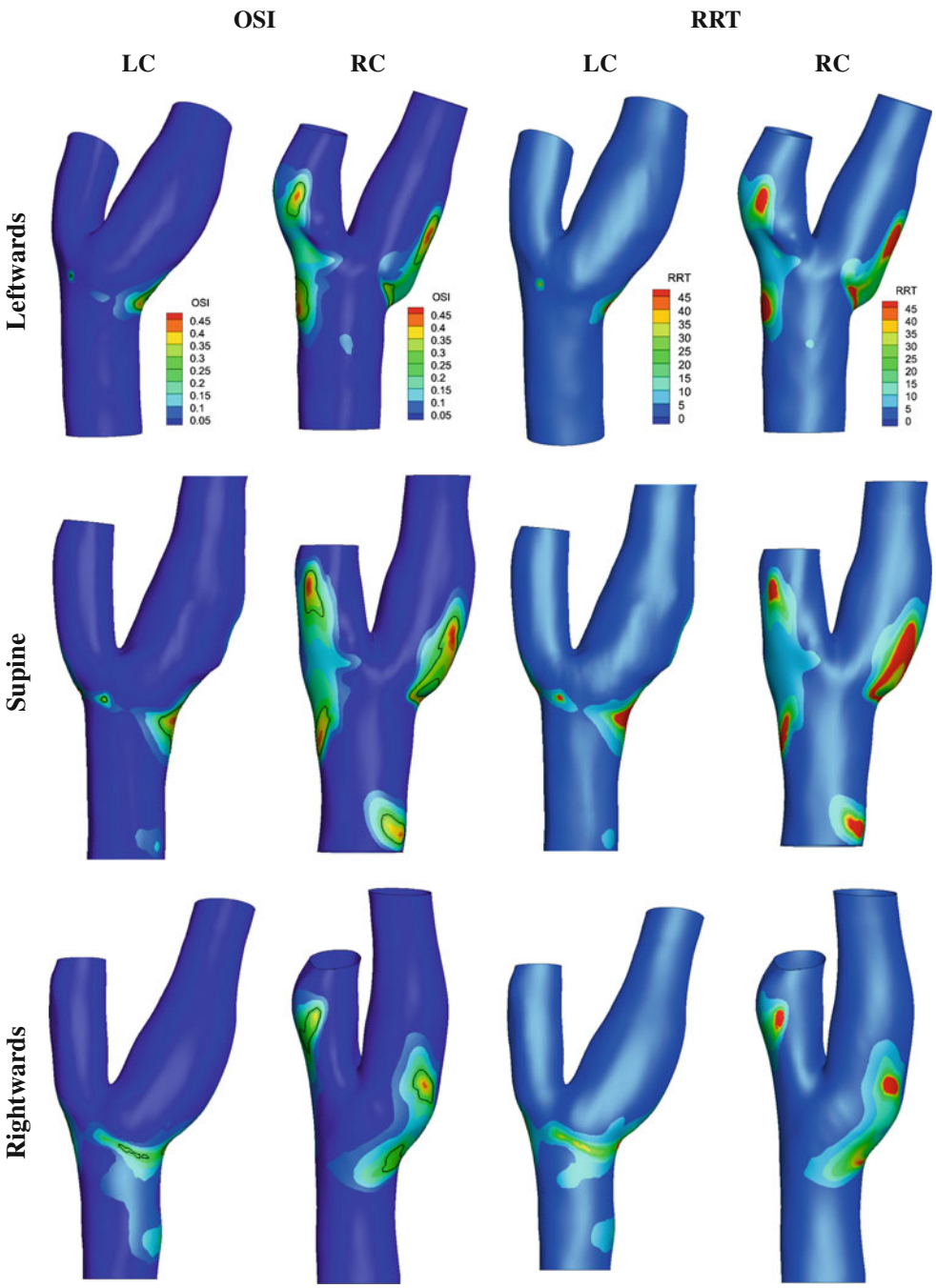

Fig. 6 *Contour plots* of time-averaged OSI and RRT for the right and left carotid in the neutral, leftward and rightward rotated head position for the subject II. OSI = 0.238 *contour lines* are shown

found by Glor et al. [9]. The relative significance of inlet boundary conditions to the observed change in hemodynamics associated to head rotation requires further investigation.

Our results show that the marked changes in CB morphology due to head rotation affect the distribution patterns of OSI, nOSI and RRT on the CB wall. However, a correlation between patterns of change in CB morphology with changes in the hemodynamic environment could not be identified. Furthermore, the potential atherogenic impact of these changes, quantified as the wall area exposure to unfavorable hemodynamics, differed both between subjects and also between head postures for the same subject. It is thus not possible based on the results of this study to indicate a preferred head posture considering the associated atherogenic impact on the CB wall.

Recent results by Zhang et al. [34], showed a correlation between expansion of the bifurcation, measured through the CCA/ICA area ratio, and CCA/ICA colinearity, measured from the ICA angle, with local CB hemodynamics. Our results indicate that given the magnitude of the observed changes in CB geometry caused by head rotation

and the results of Zhang et al. [34], one could expect that head torsion may cause true changes in the local CB hemodynamics. However, taking into account the complexity and inherent uncertainties of the involved processes (image acquisition and processing, and numerical simulation) in quantifying the atherogenic impact, the results in Table 2 should not be surprising. Imaging is the major source of uncertainty in the series of processes involved in computing the flow field in a reconstructed subject-specific CB model [30]. Therefore, lack of sufficient imaging sensitivity results in an inability to accurately resolve small scale CB shape features that change with head rotation and affect the computed flow field. It is therefore necessary to consider a methodology shift that will bypass the high intra- and inter-individual variability and enable us to better resolve the effects of head rotation on the local hemodynamics.

The significance of our findings lies on the fact that for many individuals, there is a substantial time period with prolonged head rotation which occurs during sleep in the prone position. This may provide a long enough duration of altered flow that may influence the process of atherosclerotic development. The effect of head rotation may also be important in the study of unstable plaque and the conditions that may lead to the rupture of the fibrous cap. Mitsumori et al. [19] showed that multisequence MRI can accurately characterize the in vivo state of the carotid bifurcation fibrous cap, supporting the use of this non-invasive technique to prospectively identify vulnerable plaques. The change of hemodynamic conditions and stress distribution on the fibrous cap with head rotation may be important in the study of unstable plaque and the conditions under which the fibrous cap ruptures.

Another relevant question is how much the geometry of the stenosis changes with posture, and if in some patients the stenotic effects aggravate with head rotation. It is also important to investigate whether healthy subjects and patients with greater morphologic and hemodynamic changes between neutral, RR and LR postures are at greater risk, simply because of greater frequent changes in baseline conditions during normal activities. Finally, the implantation of stents or performance of endarterectomy in this region may benefit from prior knowledge of the hemodynamics and stress distributions for all possible postures, in order to optimize device placement and minimize the possibility of restenosis. Nitinol stent fractures at the carotid bifurcation have been reported and the role of head motion posture changes in the mechanics of fracture are unknown [32]. All these questions could be answered by extended healthy subject and patient studies at different head postures and under various physiologic and pathologic conditions.

Various simplifying modeling assumptions were introduced in this study. We applied a fixed 65/35 ICA/ECA flow split, we modeled blood as a Newtonian fluid and applied a fully developed velocity profile at the inlet. The impact of these assumptions on hemodynamics computations has been assessed in the works of: (1) Balossino et al. [4] and Moriducci et al. [20], (2) Lee and Steinman [15] and Morbiducci et al. [21], and (3) Moyle et al. [22], respectively. Although these modeling assumptions will impact the computed hemodynamics in absolute terms, their effect may not be as important in our study where results are reported in relative terms as we seek to compare differences between head postures. We also applied the same CCA flow waveform for all cases considered assuming that, based on the results of Glor et al. [9], the effect of change of head posture on mean CCA flow rate is not significant.

In our recent work [3] we examined a group of ten healthy subjects and established that there is a significant effect of head posture change on CB geometric features. In this study we selected two subjects from the same group, for further scanning, to assess the effect of both rightwards and leftwards rotation of the head on right and left CB hemodynamics. Changes in bifurcation and ICA angles with head rotation in subjects I and II were significantly above and below average, respectively, of the ten subjects included in the study. Thus, despite the small number of cases considered here, our preliminary results provide a good indication of the effects of head torsion on CB hemodynamics.

The changes found in the geometry of the carotid bifurcation due to torsion of the neck and their effect on local hemodynamics may be associated with the genesis, development and proliferation of atherosclerotic disease as well as complications in cases of significantly stenotic or stented vessels. Further research is warranted with more systematic clinical studies.

Acknowledgments This work was co-funded by the European Regional Development and the Republic of Cyprus through the Research Promotion Foundation (Project IPE/YGEIA/DYGEIA/0609/11 and DIAKRATIKES/CY-SLO/0609/01) and by grant GSRT-09FR37 of the General Secretariat for Research and Technology (GSRT), Greece.

Conflict of interest The authors have no conflict of interest related to this study.

References

1. Anayiotos AS, Jones SA, Giddens DP, Glagov S, Zarins CK (1994) Shear stress at a compliant model of the human carotid bifurcation. J Biomech Eng 116:98–106
2. Antiga L, Steinman DA (2004) Robust and objective decomposition and mapping of bifurcating vessels. IEEE Trans Med Imaging 23(6):704–713

3. Aristokleous N, Seimenis I, Papaharilaou Y, Georgiou GC, Brott BC, Eracleous E, Anayiotos AS (2011) Effect of posture change on the geometric features of the healthy carotid bifurcation. IEEE Trans Inf Technol Biomed 15(1):148–154
4. Balossino R, Pennati G, Migliavacca F, Formaggia L, Veneziani A, Tuveri M, Dubini G (2009) Computational models to predict stenosis growth in carotid arteries: which is the role of boundary conditions? Comput Methods Biomech Biomed Eng 12(1):113–123
5. Bao X, Lu C, Frangos JA (1999) Temporal gradient in shear but not steady shear stress induces PDGF-A and MCP-1 expression in endothelial cells: role of NO, NF kappa B, and egr-1. Arterioscler Thromb Vasc Biol 19:996–1003
6. Bijari PB, Antiga L, Wasserman BA, Steinman DA (2011) Scan-rescan reproducibility of carotid bifurcation geometry from routine contrast-enhanced MR angiography. J Magn Reson Imaging 33(2):482–489
7. Cheng CP, Wilson NM, Hallett RL, Herfkens RJ, Taylor CA (2006) In vivo MR angiographic quantification of axial and twisting deformations of the superficial femoral artery resulting from maximum hip and knee flexion. J Vasc Interv Radiol 17(6):979–987
8. Cho YI, Back LH, Crawford DW (1985) Experimental investigation of branch flow ratio, angle, and reynolds number effects on the pressure and flow fields in arterial branch models. J Biomech Eng 107(3):257–267
9. Glor FP, Ariff B, Hughes AD, Verdonck PR, Barratt DC, Augst AD, Thom SA, Xu XY (2004) Influence of head position on carotid hemodynamics in young adults. Am J Physiol Heart Circ Physiol 287(4):H1670–H1681
10. Glor FP, Long Q, Hughes AD, Augst AD, Ariff B, Thom SA, Verdonck PR, Xu XY (2003) Reproducibility study of magnetic resonance image-based computational fluid dynamics prediction of carotid bifurcation flow. Ann Biomed Eng 31(2):142–151
11. Gonzales RS, Wick TM (1996) Hemodynamic modulation of monocytic cell adherence to vascular endothelium. Ann Biomed Eng 24(3):382–393
12. Himburg HA, Grzybowski DM, Hazel AL, LaMack JA, Li XM, Friedman MH (2004) Spatial comparison between wall shear stress measures and porcine arterial endothelial permeability. Am J Physiol Heart Circ Physiol 286(5):H1916–H1922
13. Hoi Y, Wasserman BA, Lakatta EG, Steinman DA (2010) Effect of common carotid artery inlet length on normal carotid bifurcation hemodynamics. J Biomech Eng 132(12):121008
14. Ku DN, Giddens DP, Zarins CK, Glagov S (1985) Pulsatile flow and atherosclerosis in the human carotid bifurcation. Positive correlation between plaque location and low oscillating shear stress. Arteriosclerosis 5(3):293–302
15. Lee SW, Steinman DA (2007) On the relative importance of rheology for image-based CFD models of the carotid bifurcation. J Biomech Eng 129(2):273–278
16. Lee SW, Antiga L, Spence JD, Steinman DA (2008) Geometry of the carotid bifurcation predicts its exposure to disturbed flow. Stroke 39(8):2341–2347
17. LoGerfo FW, Nowak MD, Quist WC, Crawshaw HM, Bharadvaj BK (1981) Flow studies in a model carotid bifurcation. Arteriosclerosis 1:235–241
18. Malek AM, Alper SL, Izumo S (1999) Hemodynamic shear stress and its role in atherosclerosis. JAMA 282(21):2035–2042
19. Mitsumori LM, Hatsukami TS, Ferguson MS, Kerwin WS, Cai J, Yuan C (2003) In vivo accuracy of multisequence MR imaging for identifying unstable fibrous caps in advanced human carotid plaques. J Magn Reson Imaging 17(4):410–420
20. Morbiducci U, Gallo D, Massai D, Consolo F, Ponzini R, Antiga L, Bignardi C, Deriu MA, Redaelli A (2010) Outflow conditions for image-based hemodynamic models of the carotid bifurcation: implications for indicators of abnormal flow. J Biomech Eng 132(9):091005
21. Morbiducci U, Gallo D, Massai D, Ponzini R, Deriu MA, Antiga L, Redaelli A, Montevecchi FM (2011) On the importance of blood rheology for bulk flow in hemodynamic models of the carotid bifurcation. J Biomech 44(13):2427–2438
22. Moyle KR, Antiga L, Steinman DA (2006) Inlet conditions for image-based CFD models of the carotid bifurcation: is it reasonable to assume fully developed flow? J Biomech Eng 128(3):371–379
23. Papaharilaou Y, Doorly DJ, Sherwin SJ (2002) The influence of out-of-plane geometry on pulsatile flow within a distal end-to-side anastomosis. J Biomech 35(9):1225–1239
24. Perktold K, Resch M, Peter RO (1991) Three-dimensional numerical analysis of pulsatile flow and wall shear stress in the carotid artery bifurcation. J Biomech 24:409–420
25. Perktold K, Rappitsch G (1995) Computer simulation of local blood flow and vessel mechanics in a compliant carotid artery bifurcation model. J Biomech 28:845–856
26. Roger VL, Go AS, Lloyd-Jones DM, Adams RJ, Berry JD, Brown TM, Carnethon MR, Dai S, de Simone G, Ford ES, Fox CS, Fullerton HJ, Gillespie C, Greenlund KJ, Hailpern SM, Heit JA, Ho PM, Howard VJ, Kissela BM, Kittner SJ, Lackland DT, Lichtman JH, Lisabeth LD, Makuc DM, Marcus GM, Marelli A, Matchar DB, McDermott MM, Meigs JB, Moy CS, Mozaffarian D, Mussolino ME, Nichol G, Paynter NP, Rosamond WD, Sorlie PD, Stafford RS, Turan TN, Turner MB, Wong ND, Wylie-Rosett J, American Heart Association Statistics Committee and Stroke Statistics Subcommittee (2011) Heart disease and stroke statistics–2011 update: a report from the american heart association. Circulation 123(4):e18–e209
27. Steinman DA, Taylor CA (2005) Flow imaging and computing: large artery hemodynamics. Ann Biomed Eng 33(12):1704–1709
28. Steinman DA, Thomas JB, Ladak HM, Milner JS, Rutt BK, Spence JD (2002) Reconstruction of carotid bifurcation hemodynamics and wall thickness using computational fluid dynamics and MRI. Magn Reson Med 47(1):149–159
29. Taylor CA, Draney MT (2004) Experimental and computational methods in cardiovascular fluid mechanics. Annu Rev Fluid Mech 36:197–231
30. Thomas JB, Milner JS, Rutt BK, Steinman DA (2003) Reproducibility of image-based computational fluid dynamics models of the human carotid bifurcation. Ann Biomed Eng 31(2):132–141
31. Tsao PS, Lewis NP, Alpert S, Cooke JP (1995) Exposure to shear stress alters endothelial adhesiveness. Role of nitric oxide. Circulation 92(12):3513–3519
32. Valibhoy AR, Mwipatayi BP, Sieunarine K (2007) Fracture of a carotid stent: an unexpected complication. J Vasc Surg Int Soc Cardiovasc Surg NA 45(3):603–606
33. Yushkevich PA, Piven J, Hazlett HC, Smith RG, Ho S, Gee JC, Gerig G (2006) User-guided 3D active contour segmentation of anatomical structures: significantly improved efficiency and reliability. Neuroimage 31(3):1116–1128
34. Zhang Q, Steinman DA, Friedman MH (2010) Use of factor analysis to characterize arterial geometry and predict hemodynamic risk: application to the human carotid bifurcation. J Biomech Eng 132(11):114505